LIFT CAPABILITY PREDICTION FOR AERODYNAMIC CONFIGURATIONS

Constantin ROTARU, **Raluca Ioana EDU**

Military Technical Academy, Bucharest

Abstract: *This paper presents a mathematical model of the flow around the helicopter rotor airfoil in order to predict the lift capability. The proposed solution consists in an airfoil with filled cavity, where the filled body is a rotating cylinder. The effect on the flow around the airfoil is the generation of vortices that reduce the flow separation downstream of the cavity. The CFD results were compared with those obtained by panel method and this suggests the possibility of a delay in flow separation on the upper surface for the retreating blade. Taking into account that the advancing blade operates at low angle of attack but at high subsonic or transonic conditions, whereas the retreating blade operates at low Mach numbers and high lift coefficients, this new airfoil type could improve the lifting capability of the rotor blade and may lead to new rotors optimized for greater performances in both hover and high speed forward flight.*

Keywords: *helicopter aerodynamic, panel method, rotor blade, vortex strength.*

1. INTRODUCTION

The aerodynamic characteristics of helicopter rotor airfoils must be assessed at their actual operational Reynolds numbers and Mach numbers.

The maximum lift coefficient, $C_{l\max}$, can be used as one indicator of the significance of viscous effects.

At the low end of the practical Reynolds number range for rotors, most airfoils have relatively low values of $C_{l\max}$.

This is because the viscous forces are more determinant, the boundary layer is thicker and the flow will separate from the airfoil surface.

The maximum lift that can be developed by an airfoil when operating at a steady angle of attack is related to the type of stall characteristic of that airfoil.

At low speeds, airfoils generally fall into three static stall categories, namely thin airfoil stall, leading edge stall and trailing edge stall.

The measurements show that thin airfoil and leading edge stalls can be fairly sensitive to changes in airfoil shape, whereas trailing edge stall is insensitive.

Most conventional helicopter rotor airfoils fall into the category of trailing edge or leading edge stall types at low to moderate Mach numbers. It is also common for a mixed stall behavior to occur on some airfoils which is a stall characteristic that is not clearly one type or another [1].

Airfoils designed for helicopter applications have traditionally been obtained through a long evolutionary process in which various levels of theory and experimental measurements have been combined in the pursuit of airfoil shapes with higher values of maximum lift, better lift-to-drag ratios, lower pitching moments and higher drag divergence Mach numbers.

In general, these requirements are conflicting, making the design of general purpose rotor airfoils extremely challenging.

Instead, various families of airfoils have been developed and optimized to meet the specific needs of different parts of the rotor blade.

The use of different airfoils along the blade is made easier because of computer-aided design and composite manufacturing capability which involves only small additional costs over blade made with a single airfoil section.

The selection of airfoil sections for helicopter rotors is more difficult than for a fixed-wing aircraft because they are not point designs. For angle of attack and Mach number varying continuously at all blade elements on the rotor, one airfoil section cannot meet all the various aerodynamic requirements.

The rotor limits may be determined by either advancing blade compressibility effects or retreating blade stall. Because the onset of flow separation may limit rotor performance, there has been a great deal of emphasis in rotor design on maximizing the lifting capability of rotor airfoil sections to simultaneously alleviate both compressibility effects and retreating blade stall. The rotor design point must recognize the influence of both effects as limiting factors as well as allow sufficient margins from the stall/ compressibility boundary for perturbations in angle of attack and Mach number associated with maneuvering flight and turbulent air [2].

At higher angles of attack the adverse pressure gradients produced on the upper surface of the airfoil result in a progressive increase in the thickness of the boundary layer and cause some deviation from the linear lift versus angle of attack behavior. On many airfoils, the onset of flow separation and stall occurs gradually with increasing of angle of attack but on some airfoil (those with sharp leading edges), the flow separation may occur quite suddenly. In the stalled flow regime, the flow over the upper surface of the airfoil is characterized by a region of fairly constant static pressure. The pitching moment about ¼-chord is much more negative because with the almost constant pressure over the upper surface the center of pressure is close to mid-chord. Less lift is generated by the airfoil because of the reduction in circulation and loss of suction near the leading edge and the drag is greater. Under these separated flow conditions, steady flow no longer prevails, with turbulence and vortices being ahead alternately from the leading and trailing edges of the airfoil into the wake [3].

The envelope of rotor thrust limits is the outcome of operation on the blades of stall effects at high angle of incidence and compressibility effects at high Mach number.

As forward speed increases, maximum thrust on the retreating blade falls because of the drop in dynamic pressure and this limits the thrust achievable throughout the forward speed range.

By the converse effect, maximum thrust possible on the advancing side increases but is unrealizable because of the retreating blade restriction.

At higher speeds, as the advancing tip Mach number approaches 1.0, its lift becomes restricted by shock-induced flow separation, leading to drag or pitching moment divergence, which limits the maximum speed achievable.

Thus, the envelope comprises a limit on thrust from retreating blade stall and a limit on forward speed from advancing blade Mach effects [4].

The ability to develop computers methods in performance calculation has been a major factor in the rapid development of helicopter technology.

Results may often not be greatly different from those derived from the simple analytical formulae but the fact that the feasibility of calculation is not dependent upon making a large number of challengeable assumptions is important in pinning down a design, making comparisons with flight tests [5].

2. AIRFOIL BLADE WITH FILLED CAVITY

Two-dimensional simulations were performed for a standard NACA 2412 airfoil with and without cavity.

Both edges of the cavity are sharp in order to fix the separation point (forward edge) and to maximize the feedback loop of the shear layer (rear edge).

The cavity was filled with a rotating small cylinder for improving the circulation around the airfoil (fig. 1).

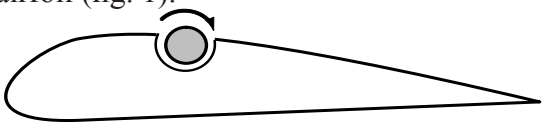

Fig. 1 Airfoil with filled cavity

The computational domain extends to a distance of 12 chords lengths in the upstream and downstream directions and three chords lengths in the upper and lower normal directions.

The distance between the discrete points at which the non-slip condition is enforced needs to be equal to or slightly greater than the grid spacing. The grid resolution and domain size were varied in order to assess convergence and influence of the far-field boundary condition.

The Reynolds number was sufficiently high such that the formation of large scale vortices and the subsequent pairing of these structures gives rise to aperiodic low frequency oscillations that are difficult to characterize because the run times are not sufficiently long to observe many periods.

The CFD results are presented in the figures 2 and 3.

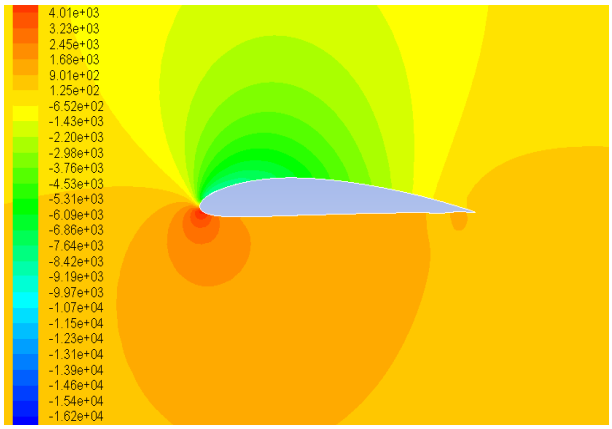

Fig. 2 Airfoil without cavity: pressure distribution

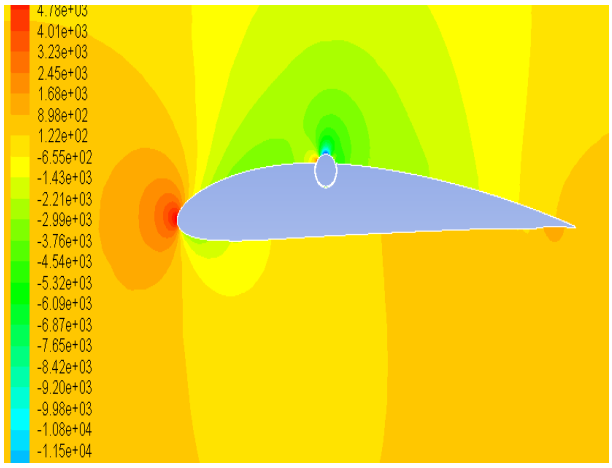

Fig. 3 Airfoil with cavity: pressure distribution

The relative high thickness of the airfoil without a cavity causes a laminar separation which initially starts approximately half a chord length from the leading edge. At very high angles of attack the flow over the airfoil with cavity separates well before the forward edge of the cavity. The separated flow displays a strong interaction with the cavity and this interaction causes the flow to shed smaller scale structures than the airfoil without cavity at the same angle of attack.

3. PANEL METHOD RESULTS

Potential flow over an airfoil of arbitrary shape can be synthesized by combining uniform flow with a curved vortex sheet wrapped around the surface of the airfoil. The concept of replacing the airfoil surface with a vortex sheet is more than just a mathematical device because there is a thin boundary layer on the surface, due to the action of friction between the surface and the airflow, in which the large velocity gradients produce substantial vorticity, hence, there is a distribution of vorticity along the airfoil surface due to viscous effects.

The vortex strength, $\gamma(s)$ must vary along the surface such that the normal component of velocity induced by the entire sheet and the uniform flow is zero everywhere along the surface of the airfoil. In most cases, the strength distribution necessary to satisfy this condition is difficult to be determined analytically. For numerical computations, such sheet can be approximated as a series of flat vortex panels wrapped around the surface of the airfoil (fig. 4).

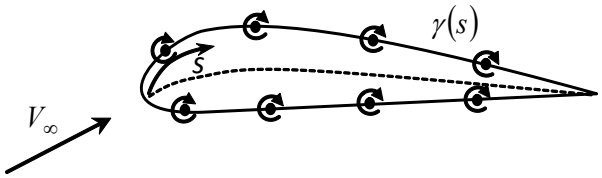

Fig. 4. Vortex sheet

To define the vortex panels, a series of nodes is placed on the airfoil surface, such that the nodes are clustered more tightly near the leading and trailing edges.

The change of variable $x/c = (1-\cos\theta)/2$ provides the desired clustering in x.

The panels start at the trailing edge, are spaced forward along the lower surface, are wrapped up around the leading edge and then run back along the upper surface to the trailing edge so that the last panel ends at the trailing edge where the first panel began.

The vortex strength $\gamma(s)$ of each panel is assumed to be linear along the panel and continuous from one panel to the next.

That is, for the n panels, the vortex panel strengths are $\gamma_1, \gamma_2, \ldots\ldots\gamma_n$, and the main thrust of the panel technique is to solve for γ_j, $j = 1$ to n, such that the body surface becomes a streamline of the flow and such that the Kutta condition $\gamma_1 = -\gamma_n$ is satisfied (fig. 5).

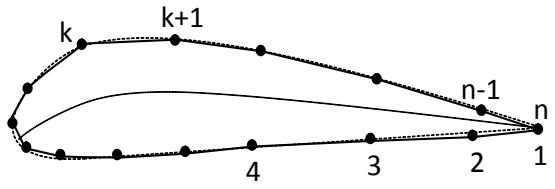

Fig. 5 Vortex panel distribution

To solve for the n unknown nodal vortex strengths, at the center of each panel is defined a control point where the normal component of the flow velocity is imposed to be zero.

For an even number n of nodes, the points x_i, $i = 1, 2, ...n/2$ on the chord line are computed from the following algorithm:

$$\delta\theta = \frac{2\pi}{n-1}, \quad x_i = \frac{c}{2}\left\{1 - \cos\left[\left(i - \frac{1}{2}\right)\delta\theta\right]\right\} \quad (1)$$

The lover and upper surface coordinates for an airfoil can be obtained from the camber line geometry, $y_c(x)$, and the thickness distribution, $t(x)$ as follows:

$$\begin{cases} X_l(x_i) = x_i + \dfrac{t(x_i)}{2\sqrt{1+\left(\dfrac{dy_c(x)}{dx}\right)^2\Big|_{x=x_i}}}\dfrac{dy_c(x)}{dx}\Big|_{x=x_i} \\ Y_l(x_i) = y_c(x_i) - \dfrac{t(x_i)}{2\sqrt{1+\left(\dfrac{dy_c(x)}{dx}\right)^2\Big|_{x=x_i}}} \end{cases} \quad (2)$$

$$\begin{cases} X_u(x_i) = x_i - \dfrac{t(x_i)}{2\sqrt{1+\left(\dfrac{dy_c(x)}{dx}\right)^2\Big|_{x=x_i}}}\dfrac{dy_c(x)}{dx}\Big|_{x=x_i} \\ Y_u(x_i) = y_c(x_i) + \dfrac{t(x_i)}{2\sqrt{1+\left(\dfrac{dy_c(x)}{dx}\right)^2\Big|_{x=x_i}}} \end{cases} \quad (3)$$

For a point x_i on the chord line (fig. 6) we have two nodes on the airfoil, one node on the lower line of the airfoil, $P_{n/2+1-i}$ and the other one on the upper line of the airfoil, $P_{n/2+i}$.

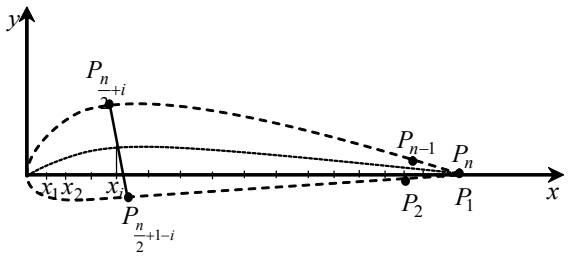

Fig. 6 The upper and lower lines nodes

A second-order panel method assumes a linear variation of $\gamma(s)$ over a given panel and the value of $\gamma(s)$ at the edges of each panel is matched to its neighbors (fig.7).

The flow-tangency boundary condition is still applied at the control point to each panel.

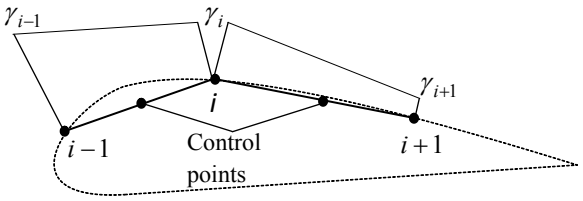

Fig. 7 Linear distribution of $\gamma(s)$

The coordinates of these control points are given by

$$\begin{cases} X_C(i) = \dfrac{X_{P_i} + X_{P_{i+1}}}{2} \\ Y_C(i) = \dfrac{Y_{P_i} + Y_{P_{i+1}}}{2} \end{cases} \quad (4)$$

Each panel is assigned a local panel coordinate system (ξ, η) as shown in fig. 8.

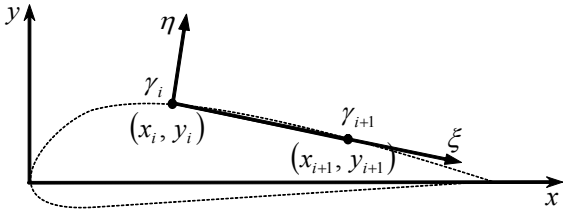

Fig. 8 Vortex panel coordinate system

For each panel, an infinite number of infinitesimally weak vortices are combined in side-by-side fashion as shown in fig. 9.

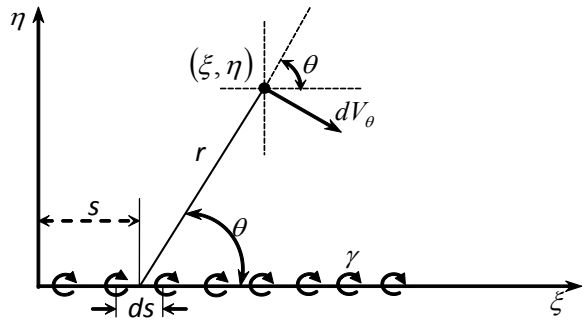

Fig. 9 Edge view of a 2-D vortex panel

Consider a differential segment of a vortex panel that lies on the ξ axis at the location $\xi = s$ and has length ds.

The velocity induced at any point (ξ, η) by this differential vortex is normal to the vector $\vec{r}$ and has a magnitude inversely proportional to the distance between the points of coordinates $(s, 0)$ and (ξ, η), namely $r = |\vec{r}|$. The ξ- and η- components of the velocity induced at the point (ξ, η) by this infinitesimally vortex panel are given by

$$\begin{cases} dV_\xi = dV_\theta \sin\theta = \dfrac{\gamma(s)}{2\pi r}\sin\theta\, ds \\ dV_\eta = -dV_\theta \cos\theta = -\dfrac{\gamma(s)}{2\pi r}\cos\theta\, ds \end{cases} \tag{5}$$

According to fig. 9 we have

$$\begin{cases} \sin\theta = \dfrac{\eta}{r} \\ \cos\theta = \dfrac{\xi - s}{r} \end{cases} \tag{6}$$

where $r = \sqrt{(\xi - s)^2 + \eta^2}$.

It follows that

$$\begin{cases} dV_\xi = \dfrac{\eta\,\gamma(s)}{2\pi\left[(\xi - s)^2 + \eta^2\right]} ds \\ dV_\xi = -\dfrac{((\xi - s))\gamma(s)}{2\pi\left[(\xi - s)^2 + \eta^2\right]} ds \end{cases} \tag{7}$$

A linear vortex strength distribution on the panel j extending from $\xi = 0$ to $\xi = l_j$ has the expression

$$\gamma(s) = \frac{\gamma_{j+1} - \gamma_j}{l_j} s + \gamma_j \tag{8}$$

where

$$l_j = \sqrt{(x_{j+1} - x_j)^2 + (y_{j+1} - y_j)^2} \tag{9}$$

The matrix of the velocities V_ξ and V_η is

$$\begin{bmatrix} V_\xi \\ V_\eta \end{bmatrix} = \frac{1}{2\pi l_j}\begin{bmatrix} (l_j - \xi)B + \eta A & \xi B - \eta A \\ -l_j - (l_j - \xi)A + \eta B & l_j - \xi A - \varepsilon B \end{bmatrix} \cdot \begin{bmatrix} \gamma_j \\ \gamma_{j+1} \end{bmatrix}$$

where

$$\begin{cases} A = \dfrac{1}{2} h\, \dfrac{\xi^2 + \eta^2}{(\xi - l_j)^2 + \eta^2} \\ B = \arctan\dfrac{l_j - \xi}{\eta} + \arctan\dfrac{\xi}{\mu} \end{cases} \tag{10}$$

In order to get the velocity induced by panel j at the control point of the panel i, the coordinates of control point must be expressed from the coordinate system (x, y) in the coordinate system (ξ, η) of panel j, making a rotation with angle β_j and a translation in the point (x_j, y_j) as it follows

$$\begin{cases} \sin\beta_j = \dfrac{y_{j+1} - y_j}{l_j} \\ \cos\beta_j = \dfrac{x_{j+1} - x_j}{l_j} \end{cases} \tag{11}$$

$$\begin{bmatrix} \xi_C(i) \\ \eta_C(i) \end{bmatrix} = \begin{bmatrix} \cos\beta_j & \sin\beta_j \\ -\sin\beta_j & \cos\beta_j \end{bmatrix} \cdot \begin{bmatrix} x_C(i) - x_j \\ y_C(i) - y_j \end{bmatrix} \tag{12}$$

$$\begin{bmatrix} V_x(i) \\ V_y(i) \end{bmatrix} = \begin{bmatrix} P_1(j,i) & P_2(j,i) \\ P_2(j,i) & P_2(j,i) \end{bmatrix} \cdot \begin{bmatrix} \gamma_j \\ \gamma_{j+1} \end{bmatrix} \tag{13}$$

The velocity $V_\eta(i)$ induced in the control point of panel i by panel j is

$$V_\eta(i) = \left(-\frac{y_{i+1} - y_i}{l_i} P_1(j,i) + \frac{x_{i+1} - x_i}{l_i} P_2(j,i)\right)\gamma_i + \left(-\frac{y_{i+1} - y_i}{l_i} P_2(j,i) + \frac{x_{i+1} - x_i}{l_i} P_2(j,i)\right)\gamma_{i+1}$$

The $n \times n$ airfoil coefficient matrix M is generated from the 2×2 panel coefficient matrix in airfoil coordinates, $P(i, j)$ for the velocity induced at the control point i by panel j, extending from node j to node $j+1$, and the n nodal vortex strengths, γ_1 through γ_n are then obtained by numerically solving the linear system

$$M \cdot \begin{bmatrix} \gamma_1 \\ \gamma_2 \\ ... \\ \gamma_{n-1} \\ \gamma_n \end{bmatrix} = V_\infty \begin{bmatrix} [(y_2 - y_1)\cos\alpha - (x_2 - x_1)\sin\alpha]/l_1 \\ [(y_3 - y_2)\cos\alpha - (x_3 - x_2)\sin\alpha]/l_2 \\ ..... \\ [(y_n - y_{n-1})\cos\alpha - (x_n - x_{n-1})\sin\alpha]/l_{n-1} \\ 0.0 \end{bmatrix}$$

Once the nodal strengths are known, the velocity and pressure at any point in space can be computed by adding the velocity induced by all $n-1$ vortex panels in the free stream velocity,

$$\begin{bmatrix} V_x \\ V_y \end{bmatrix} = V_\infty \begin{bmatrix} \cos\alpha \\ \sin\alpha \end{bmatrix} + \sum_{i=1}^{n-1} \begin{bmatrix} V_x(i) \\ V_y(i) \end{bmatrix} \quad (14)$$

The lift coefficient for the entire airfoil is the sum of those induced by all the $n-1$ panels,

$$C_l = \sum_{i=1}^{n-1} \frac{l_i}{c} \cdot \frac{\gamma_i + \gamma_{i+1}}{V_\infty} \quad (15)$$

3. RESULTS

For the clean airfoil at $\alpha = 0^\circ$ the flow initially separates around 50% of the chord length and this separation causes a periodic vortex shedding in the wake of the airfoil. At $\alpha = 10^\circ$ and $\alpha = 15^\circ$ the separation bubble and the vortex structures are larger and the separation point on the suction side moves upstream with increasing the angle of attack. The separated vortices tend to merge into larger structures before being shed into the wake.

The filled cavity has a strong influence on the structure of the flow in the separation bubble. It promotes smaller-scale vortex shedding than would otherwise occur for the airfoil without a cavity at the same angle of attack.

CONCLUSIONS

The section lift coefficients predicted by thin airfoil theory and panel codes are in good agreement with experimental data for low Mach numbers and small angles of attack.

The airfoil with filled cavity gives good results regarding the maximum lift coefficient and the behavior of the helicopter retreating blade.

BIBLIOGRAPHY

1. Gordon Leishman, *Principles of Helicopter Aerodynamics,* Cambridge University Press (2007).
2. Katz J, Plotkin, A., *Low-Speed Aerodynamics*, second edition, Cambridge University Press (2010)
3. Prouty, R. *Helicopter Performance, Stability and Control,* Krieger Publishing Company, Florida, USA (2002).
4. Rotaru, C., Circiu, I., Boscoianu M. *Computational Methods for the Aerodynamic Design*, Review of the Air Force Academy, No 2(17), p. 43-48 (2010).
5. Rotaru, C., Arghiropol A., *Maple soft solutions for nonlifting flows over arbitrary bodies,* Proceedings of the 3rd WSEAS international conference on FINITE DIFFERENCES - FINITE ELEMENTS - FINITE VOLUMES - BOUNDARY ELEMENTS, ISSN 1970-2769, p. 270-274 (2010).